MATERIALS CHEMISTRY FRONTIERS

RESEARCH ARTICLE

View Article Online
View Journal

Cite this: DOI: 10.1039/d5qm00520e

Color-tunable, high-dissymmetry circularly polarized phosphorescence in chiral nematic phases: self-assembly, energy transfer, and handedness inversion

Jung-Moo Heo, [a] Jihyun Park[b] and Jinsang Kim *[abcd]

Purely organic circularly polarized phosphorescence (CPP) materials are promising candidates for chiral optoelectronic and photonic applications but remain limited by challenges in achieving both high quantum efficiency and strong dissymmetry. Here, we report a high-performance CPP system based on brominated cholesteric liquid-crystalline (CLC) molecules that spontaneously self-assemble into left-handed chiral nematic (N*) phases. Among the series, **Br10Ch** exhibits bright blue CPP at 450 nm with a phosphorescent quantum yield of 36% and a dissymmetry factor of g_{lum} = +0.30, enabled by enhanced spin–orbit coupling and long-range helical ordering that suppress non-radiative decay. Furthermore, doping the N* matrix with an achiral fluorescent dye (8CNS) enables triplet-to-singlet Förster resonance energy transfer, yielding green circularly polarized fluorescence at 502 nm with inverted handedness (g_{lum} = −0.32) *via* selective reflection within the cholesteric host. This combined color tunability and handedness switching in a purely organic system provides a modular approach for tailoring chiroptical emission without heavy metals. Our findings establish CLCs as versatile supramolecular scaffolds for high-performance CPP, offering new opportunities for dynamic optical control in displays, data encryption, and advanced photonic devices.

Received 17th July 2025,
Accepted 18th September 2025

DOI: 10.1039/d5qm00520e

rsc.li/frontiers-materials

Introduction

Purely organic materials exhibiting circularly polarized luminescence (CPL) have garnered increasing attention due to their potential applications in advanced optoelectronics,[1,2] chiral recognition,[3,4] optical imaging,[5,6] and asymmetric catalysis.[7,8] To maximize CPL performance, it is essential to simultaneously enhance both the luminescence quantum yield (Φ) and the luminescence dissymmetry factor ($|g_{lum}|$), the latter quantifying the degree of circular polarization.[9,10] However, enhancing both Φ and $|g_{lum}|$ concurrently remains a considerable challenge due to an inherent trade-off between brightness and polarization purity.[9]

While circularly polarized fluorescence (CPF) has been extensively studied, achieving efficient circularly polarized phosphorescence (CPP) at room temperature using purely organic systems remains significantly more challenging. This difficulty stems from the spin-forbidden nature between the singlet and triplet transition responsible for room temperature phosphorescence (RTP),[11] which is inherently hindered in organic systems by weak spin–orbit coupling (SOC) and exacerbated by non-radiative losses due to molecular vibrations[12–15] and oxygen quenching.[16–18] To overcome these limitations, strategies such as crystal engineering,[19–22] polymer rigidification,[23–26] supramolecular self-assembly,[15,27–29] and host–guest doping[30–33] have been employed to stabilize triplet excitons and enhance SOC. Despite these advances, purely organic CPP systems generally exhibit low dissymmetry factors ($|g_{lum}|$ ~10^{-4}–10^{-2}), clearly underscoring the persistent difficulty in simultaneously achieving high quantum efficiency and significant circular polarization. Noteworthy progress has emerged in recent years. For instance, An *et al.* reported ionization-induced assemblies formed by confining organic phosphors with chiral counterions, achieving a high Φ of 43.2% and a $|g_{lum}|$ value of 0.13.[19] Similarly, Huang *et al.* developed a covalently self-confined chiral chromophore embedded in a polymer matrix, which exhibited blue emission at 414 nm, a prolonged lifetime of 3.0 s, and a dissymmetry factor on the order of 10^{-2}.[34]

Cholesteric liquid crystals (CLCs), also known as chiral nematic liquid crystals (N* LCs), offer a powerful platform for

[a] Department of Materials Science and Engineering, University of Michigan, Ann Arbor, Michigan 48109, USA
[b] Department of Chemistry, University of Michigan, Ann Arbor, Michigan 48109, USA
[c] Macromolecular Science and Engineering, University of Michigan, Ann Arbor, Michigan 48109, USA
[d] Biointerfaces Institute, University of Michigan, Ann Arbor, Michigan 48109, USA. E-mail: jinsang@umich.edu

enhancing CPP performance.[35–44] Their intrinsic helical superstructures promote long-range molecular alignment, which not only amplifies CPL signals but also suppresses non-radiative decay. The CPL generation mechanism in N* LCs generally operates *via* two distinct modes: (1) optical rotation, where CPL follows the helical twist of the N* LC axis, leading to chirality amplification along the propagation direction; and (2) selective reflection, where CPL with the same handedness as the helical structure is reflected while the opposite-handed CPL is transmitted, enabling handedness inversion depending on the spectral overlap between emission and the reflection band.[35,36]

Recent efforts incorporating N* LCs have led to significant advancements in CPP systems. For example, Deng *et al.* employed a polymer matrix in combination with a cholesteric LC layer to achieve multicolor circularly polarized room-temperature phosphorescence, reporting a high $|g_{lum}|$ of up to 1.57 and an ultralong lifetime of 18 s.[36] Similarly, Ma *et al.* demonstrated a photon-coupling strategy achieving multicolor CP afterglow with lifetimes exceeding 6 seconds and $|g_{lum}|$ values reaching 1.90.[37] Nonetheless, a general design strategy that unifies high Φ and high $|g_{lum}|$ in a single organic material remains elusive.

Building upon these advances, we report a CPP system that merges a phosphorescent chromophore core with a cholesteric LC motif. The molecular design, Br(*n*)Ch (*n* = 6, 10, 14; Fig. 1a), features brominated 2,5-dialkoxyterephthalate cores that not only enhance SOC through heavy atom effects and efficient n–π mixing (El-Sayed rule) but also drive spontaneous formation of left-handed N* LC (Fig. 1b and e). Among the series, **Br10Ch** exhibits bright left-handed blue CPP at 450 nm with a high

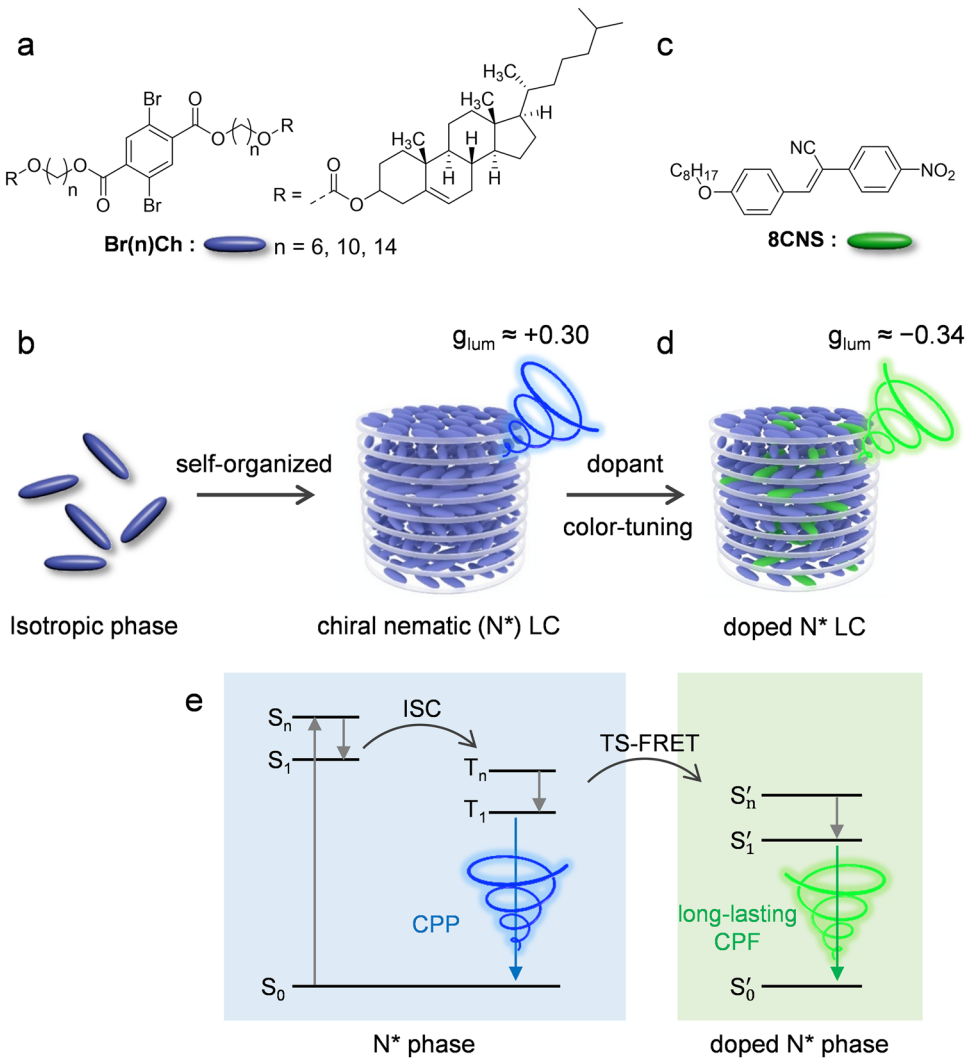

Fig. 1 Molecular components and chiroptical emission pathways in cholesteric liquid crystalline systems. (a) Chemical structure of Br(*n*)Ch (*n* = 6, 10, 14), a brominated mesogen designed to form chiral nematic (N*) phases. (b) Br(*n*)Ch self-assembles into N* liquid crystals, exhibiting circularly polarized phosphorescence (CPP) with a dissymmetry factor of $g_{lum} \approx +0.30$. (c) Structure of the achiral fluorescent dye 8CNS used as an energy acceptor. (d) Doping with 8CNS enables triplet-to-singlet Förster resonance energy transfer (TS-FRET), producing green circularly polarized fluorescence (CPF) with reversed handedness ($g_{lum} \approx -0.34$). (e) Schematic illustration of the excited-state processes: ISC leads to CPP in the pristine N* phase, while TS-FRET enables CPF in the doped system.

dissymmetry factor (g_{lum} = +0.30) and room-temperature phosphorescence quantum yield (Φ_{PH} = 36%), attributed to the combined effects of enhanced SOC and long-range helical order enabled by optical rotation.[35]

Furthermore, we show that doping **Br10Ch** with an achiral fluorophore (8CNS; Fig. 1c) facilitates triplet-to-singlet Förster resonance energy transfer (TS-FRET; Fig. 1e),[45] resulting in long-lasting green CPF at 502 nm in Fig. 1d. Notably, this process leads to an inversion in CPL handedness (g_{lum} = −0.32), which we attribute to selective reflection within the N* LC matrix. In this scenario, left-handed CPL is reflected while right-handed CPL is transmitted, due to the spectral overlap between emission and reflection bands.[35] These results underscore the versatility of cholesteric liquid crystal frameworks as a tunable platform for developing purely organic CPP emissive materials.

Results

Liquid crystalline phase behavior

The mesophase behavior of Br(n)Ch (n = 6, 10, 14) was characterized using differential scanning calorimetry (DSC) and polarized optical microscopy (POM). DSC thermograms were obtained during the second heating and cooling cycles at 5 °C min^{-1} to assess thermotropic liquid crystalline properties (Fig. 2a–c). All compounds exhibited two distinct exothermic transitions upon cooling, along with a glass transition (T_g), characteristic of cholesteric mesogens.[46] Specifically, **Br6Ch** displayed transitions at 119 °C, 73 °C, and T_g at 20 °C; **Br10Ch** at 84 °C, 61 °C, and T_g at 7 °C; and **Br14Ch** at 92 °C, 43 °C, and T_g at 6 °C. **Br6Ch** and **Br10Ch** showed reversible phase transitions, while **Br14Ch** exhibited irreversible behavior with broadened features—likely due to increased chain entanglement and conformational disorder associated with its longer alkyl chains.

To correlate thermal transitions with mesophase structures, POM images were collected during cooling from 150 °C at 5 °C min^{-1} (Fig. 2d–i and Fig. S1–S3). Textures indicative of nematic (N) phases appeared near the first exothermic transitions: ∼80 °C for **Br6Ch**, ∼70 °C for **Br10Ch**, and ∼60 °C for **Br14Ch**. Upon further cooling, fingerprint textures characteristic of chiral nematic (N*) phases emerged at ∼30 °C (**Br6Ch**), ∼25 °C (**Br10Ch**), and ∼25 °C (**Br14Ch**).[46] **Br10Ch** displayed uniform and well-defined fingerprint patterns, while **Br14Ch** showed dark and irregular domains, suggesting disrupted helical alignment. These observations are consistent with the broadened and irreversible DSC signals of **Br14Ch** and highlight the impact of alkyl chain length on mesophase order. No additional phase transitions were observed

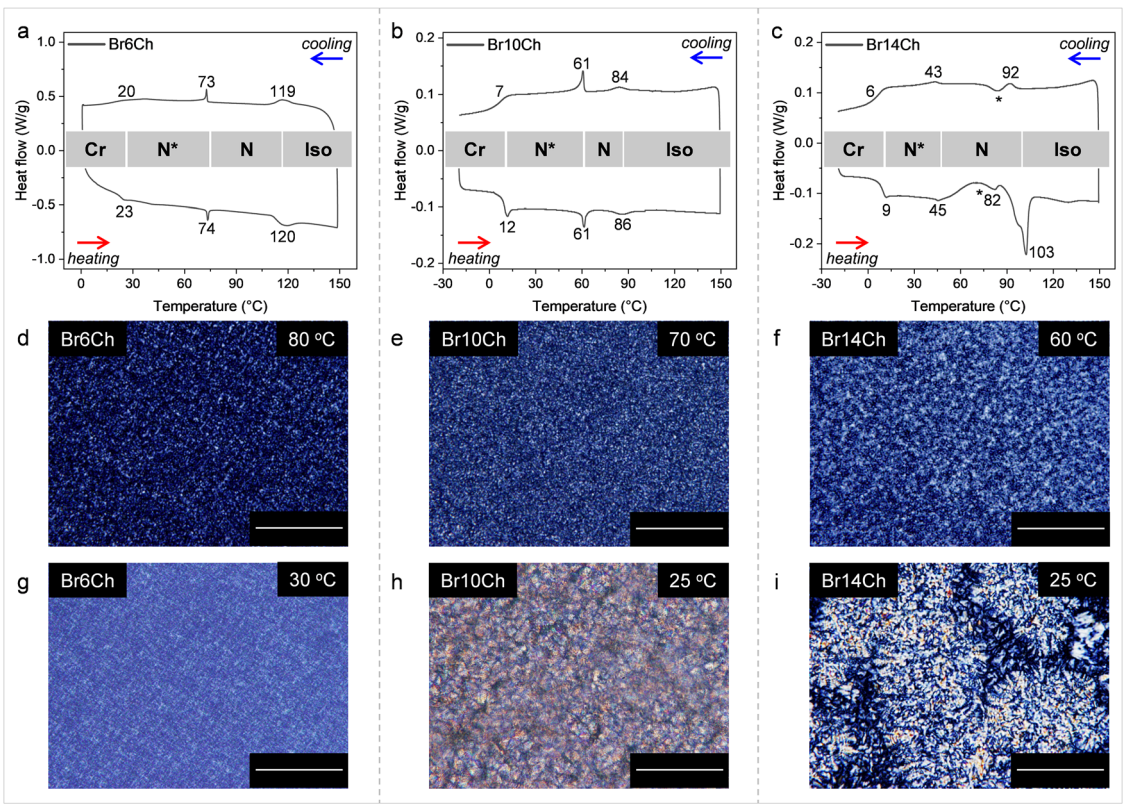

Fig. 2 Characterization of self-assembled liquid crystalline phases *via* thermal and optical methods. (a)–(c) Differential scanning calorimetry (DSC) profiles of **Br6Ch**, **Br10Ch**, and **Br14Ch** during heating and cooling at 5 °C min^{-1}, showing phase transitions among crystalline (Cr), chiral nematic (N*), nematic (N), and isotropic (Iso) states. Asterisks denote transitions not clearly observed in polarized optical microscopy (POM). (d)–(f) POM images of **Br6Ch**, **Br10Ch**, and **Br14Ch** in the nematic (N) phase. (g)–(i) Corresponding POM images in the chiral nematic (N*) phase, all acquired during cooling at 5 °C min^{-1}. Scale bars: 50 μm.

below T_g, indicating vitrification into a solid glassy or crystalline state.

Collectively, the Br(n)Ch compounds form two distinct thermotropic mesophases—N and N*—with **Br10Ch** demonstrating superior phase order and stability (see Fig. 2 and Table 1). This ordered molecular organization provides an optimal environment for suppressing non-radiative pathways and supporting efficient circularly polarized phosphorescence (CPP).

Optical behavior

Photophysical properties of the Br(n)Ch series were evaluated in dilute chloroform solution (10^{-5} M) at both room temperature (298 K, RT) and low temperature (80 K, LT). As shown in Fig. 3a and Fig. S4a–c, all compounds displayed similar absorption maxima at 307 nm, attributed to the 2,5-dibromoterephthalate core. At room temperature, no photoluminescence was detectable due to rapid non-radiative decay pathways. However, upon cooling to 80 K, strong emission emerged at 448 nm, as the rigidified frozen matrix effectively suppressed non-radiative relaxation, facilitating efficient intersystem crossing and prominent emission from the triplet state.[47] This emission spectrum closely overlapped with the delayed emission profiles (delay time: 0.2–1.0 ms), confirming its phosphorescent nature originating from triplet excited states. The measured emission lifetime (τ_{ph}) was ~1.1 ms, supporting the triplet origin of the emission in the frozen solution (Fig. S4d).[47,48]

To investigate room-temperature phosphorescence (RTP) in condensed phases, thin films (~20 μm) of the Br(n)Ch compounds were fabricated between quartz substrates under their N* phases. As shown in Fig. 3b and c, all three compounds exhibited RTP at ~450 nm, with emission profiles matching delayed emission spectra (Fig. S5), confirming a triplet-state origin. The absence of fluorescence signals and the presence of bromine suggest efficient ISC through heavy atom effect. Notably, RTP intensity varied markedly with alkyl chain length, reflecting differences in mesophase organization.

Phosphorescence lifetimes (τ_{PH}) and absolute quantum yields (Φ_{PH}) were measured, from which radiative (k_{PH}) and non-radiative (k_{nr}) rate constants were derived (Table 2). As shown in Fig. 3d, the degree of N* phase order strongly influenced RTP efficiency. **Br10Ch**, which formed highly ordered N* structures, showed the highest performance (Φ_{PH} = 36%, τ_{PH} = 45 μs), with $k_{PH} = 9.0 \times 10^3$ s^{-1} and $k_{nr} = 1.6 \times 10^4$ s^{-1}. **Br6Ch**, with moderate N* order, had Φ_{PH} = 12% and τ_{PH} = 13 μs, while **Br14Ch**, with disrupted mesophase alignment, showed the lowest efficiency (Φ_{PH} = 4%, τ_{PH} = 10 μs). **Br14Ch** also exhibited the highest non-radiative decay rate ($k_{nr} = 9.6 \times 10^4$ s^{-1}), consistent with its irregular supramolecular packing. These data confirm a direct correlation between mesophase order and RTP performance in the Br(n)Ch series.

To support the experimentally observed RTP behavior, time-dependent density functional theory (TD-DFT) calculations were performed on the core chromophore of **Br10Ch**, 2,5-dibromoterephthalate (Fig. 3e). Single-crystal structures could not be obtained due to the soft, liquid crystalline nature of the material. Therefore, the ground-state geometry was optimized using DFT, followed by TD-DFT calculations. Natural transition orbital (NTO) analysis revealed significant angular momentum transfer localized on carbonyl oxygen and bromine atoms, corresponding to a transition from the S_1 (π,π^*) state at 3.97 eV to the T_3 (n,π^*) state at 4.00 eV—consistent with El-Sayed's rule (Fig. 3e).[11] Furthermore, a large spin–orbit coupling (SOC) matrix element (~345 cm^{-1}) was calculated for the S_1–T_3 transition, suggesting a highly efficient ISC channel (Fig. 3e).[11] These theoretical findings are in strong agreement with the observed RTP behavior and confirm that the **Br10Ch** core structure is well-suited for triplet state formation *via* enhanced SOC.

Chiroptical properties of N* phase

To probe the helical superstructure and chiroptical behavior of the N* phase formed by **Br10Ch** at room temperature, circular dichroism (CD) and CPL measurements were conducted on thin films cast between quartz substrates. As shown in Fig. 4a, **Br10Ch** exhibited a strong positive CD signal beyond 350 nm, characteristic of a left-handed cholesteric mesophase. This response is attributed to the long-range helical ordering of the N* LC phase, which efficiently amplifies molecular chirality at the supramolecular level. We next examined the CPP behavior of **Br10Ch** at room temperature. As shown in Fig. 4b, **Br10Ch** displayed intense left-handed CPL emission centered at 460 nm, coinciding with its phosphorescence maximum. The dissymmetry factor (g_{lum}) reached +0.30, indicating highly efficient circular polarization of triplet-state emission. This strong chiroptical response arises from the synergistic effects of enhanced SOC, efficient ISC, and the helical amplification effect of the left-handed N* phase. As illustrated in Fig. 4c, the observed optical rotation and emission helicity are consistent with the structural handedness of the N* phase, supporting the interpretation that the emitted CPL propagates along the helical axis and retains its handedness.[35] Together, these results establish **Br10Ch** as a rare example of a purely organic material exhibiting bright, left-handed blue CPP emission (450 nm, g_{lum} = +0.30, Φ_{PH} = 36%) under ambient conditions.[15]

Tunable circularly polarized emission *via* TS-FRET doping

To further exploit the CPP-active matrix, we investigated emission color tuning through triplet-to-singlet Förster resonance energy transfer (TS-FRET)[45,49] by doping **Br10Ch** with an achiral fluorescent dye, 8CNS (Fig. 5a), exhibiting strong green fluorescence in the aggregated state, with a maximum at 512 nm (Fig. S6). The thermal and mesophase behavior of the doped system

Table 1 Phase transition temperatures of the investigated compounds determined by DSC and POM analyses

Cooling at 5 °C min^{-1}			
Compound	Iso to N (°C)	N → N* (°C)	N* → Cr (°C)
Br6Ch	119	73	20
Br10Ch	84	61	7
Br14Ch	92	43	6

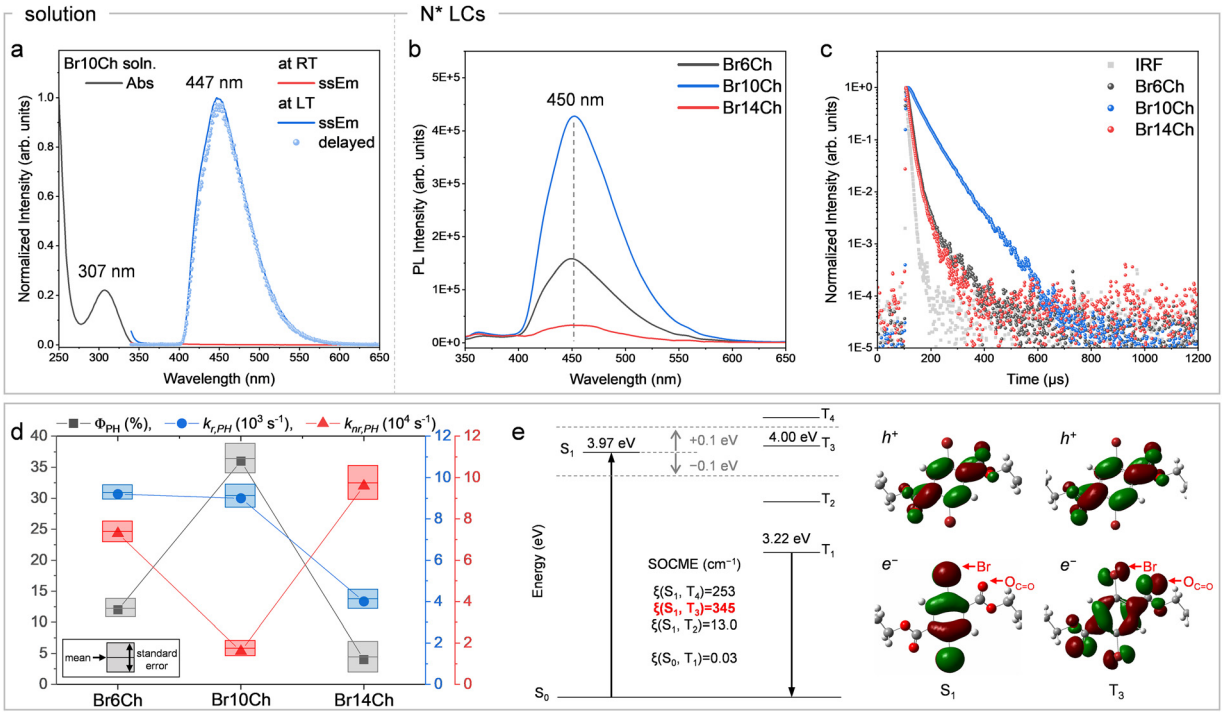

Fig. 3 Photophysical properties of Br(*n*)Ch in solution and chiral nematic (N*) liquid crystal phases. (a) Absorption and emission spectra of **Br10Ch** in solution at room temperature (298 K, RT) and low temperature (80 K, LT). No emission is observed at RT, while clear phosphorescence appears at LT, overlapping with the delayed emission spectrum (0.2–1.0 ms), confirming triplet-state emission. (b) and (c) Phosphorescence spectra and lifetimes of **Br6Ch**, **Br10Ch**, and **Br14Ch** in N* LCs at RT, showing chain-length-dependent emission behavior. (d) Comparison of phosphorescence quantum yield (Φ_{PH}) radiative rate constant (k_{PH}), and non-radiative rate constant (k_{nr}) across the series. (e) TD-DFT-derived Jablonski diagram and natural transition orbital (NTO) analysis for the **Br10Ch** chromophore, indicating efficient ISC from S_1 (π, π^*) to T_3 (n, π^*) *via* El-Sayed's rule.

(1 wt% 8CNS in **Br10Ch**) was first investigated. DSC analysis (Fig. S7) revealed phase transition temperatures slightly lower than the pristine **Br10Ch** (84 °C → 54 °C → T_g = 7 °C), indicating minimal disruption of the doped N* LC. POM observations (Fig. S8) showed that, after the first exothermic event, focal conic textures emerged.[46] Upon further cooling, oily streak textures characteristic of well-formed doped N* phases developed, confirming that cholesteric order is retained despite the presence of the dopant.[46]

Photophysically, doping with 8CNS resulted in the complete replacement of **Br10Ch** phosphorescence at 452 nm with a new emission band at 502 nm, exhibiting a high Φ of 74% (Fig. 5b). This emission spectrum closely matched the delayed emission spectrum (0.2–1.0 ms delay) when excited at 307 nm, corresponding to the absorption maximum of **Br10Ch**, thereby confirming highly efficient TS-FRET from the host to 8CNS. The TS-FRET efficiency (E) was calculated using $E = 1-(\tau_{DA}/\tau_D)$, where τ_D is the donor lifetime in the absence of acceptor (45 μs for undoped **Br10Ch**) and τ_{DA} is the donor lifetime in the presence of acceptor.[50] Nearly complete quenching of **Br10Ch** emission (Fig. 5b) indicated $\tau_{DA} \ll \tau_D$, yielding an efficiency approaching unity ($E \approx 1$). Time-resolved photoluminescence measurements further supported this, revealing a long-lived emission component with a lifetime of ~110 μs (Fig. S9), characteristic of triplet-sensitized fluorescence. Furthermore, a significant shift in the CIE coordinates from (0.147, 0.122) to (0.260, 0.510) demonstrates effective and tunable color modulation of the circularly polarized emission (Fig. 5c). To disentangle the contribution from direct excitation of 8CNS, we also evaluated the photoluminescence of doped PMMA films. When excited at 307 nm, the film exhibited emission at 497 nm with a short lifetime of ~1.5 ns (Fig. S10), consistent with direct fluorescence from 8CNS due to its broad absorption (Fig. S6). These results indicate that the observed high Φ in the doped N* LC arises from a dual mechanism—both direct excitation of 8CNS and TS-FRET from **Br10Ch**.

Chiroptically, the CD spectrum of the doped N* LC retained a strong positive signal but exhibited a pronounced red shift in the selective reflection band—from 350–400 nm in the undoped N* LC (Fig. 4a) to 450–500 nm in the doped system (Fig. 5d)—indicating an increased helical pitch caused by guest-

Table 2 Photophysical properties of Br(*n*)Ch in the N* phases. The table lists the emission maximum (λ_{PH}), phosphorescence quantum yield (Φ_{PH}), phosphorescence lifetime (τ_{PH}); the radiative and nonradiative decay rates k_{PH}, k_{nr} where obtained *via* $k_{PH} = \Phi_{PH}/\tau_{PH}$ and $k_{nr} = (1-\Phi_{PH})/\tau_{PH}$, assuming an ISC efficiency h_{ISC} = 1

Compounds	λ_{PH} (nm)	Φ_{PH} (%)[a]	τ_{PH} (μs)[b]	k_{PH} (10^3 s^{-1})	k_{nr} (10^3 s^{-1})
Br6Ch	449	12	13	9.2	73
Br10Ch	452	36	45	9	16
Br14Ch	452	4	10	4	96

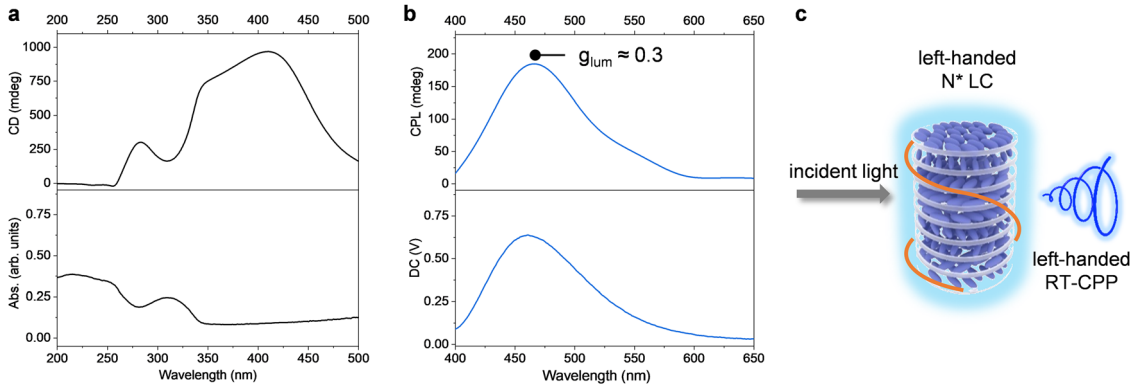

Fig. 4 Chiroptical properties and circularly polarized phosphorescence (CPP) behavior of **Br10Ch** in the N phase. (a) Circular dichroism (CD, top) and UV-vis absorption (bottom) spectra of **Br10Ch** in the N* LC phase, confirming strong chiral ordering. (b) Circularly polarized luminescence (CPL, top) spectra with corresponding g_{lum} of **Br10Ch** in the N* LC phase, showing intense left-handed CPP. (c) Schematic illustration of the left-handed N* LC structure generating left-handed CPP under incident light.

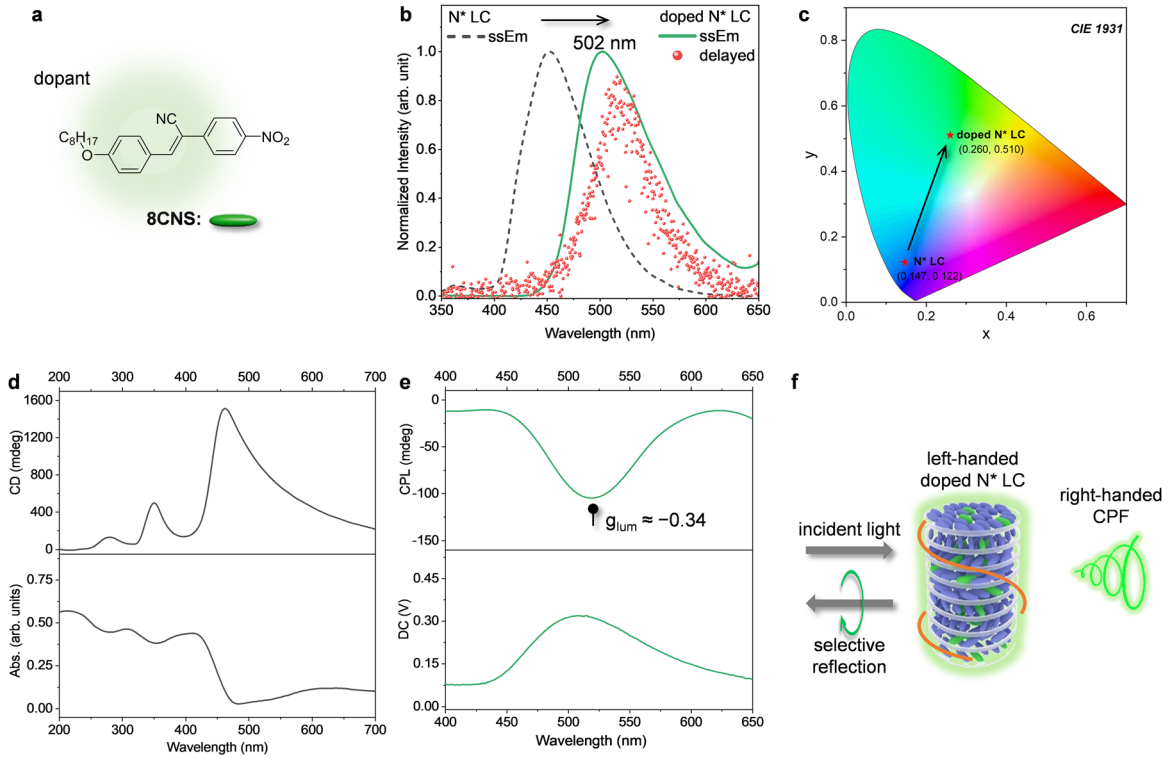

Fig. 5 Emission color tuning and inversion of circular polarization in doped chiral nematic liquid crystals. (a) Chemical structure of the achiral fluorescent dopant 8CNS. (b) ssEm and delayed emission spectra of **Br10Ch**-based N* LC before and after doping with 8CNS. After doping, the emission red-shifts to 502 nm, indicating efficient triplet-to-singlet Förster resonance energy transfer (TS-FRET). (c) CIE 1931 chromaticity diagram showing a clear color shift from blue (N* LC) to green (doped N* LC). (d) CD and UV-vis absorption spectra of doped N* LC, confirming the retention of chiral structure. (e) CPL with corresponding dissymmetry factor (g_{lum}) spectra of the doped N* LC, showing strong right-handed circularly polarized fluorescence (CPF) with $g_{lum} \approx -0.34$. (f) Schematic illustration showing that in the left-handed N* LC, left-handed CPL is selectively reflected, while right-handed CPL is transmitted, resulting in right-handed CPF from the doped LC system.

induced swelling of the cholesteric lattice.[48] In Fig. 5e, remarkably, the CPL spectrum of the doped sample showed a pronounced negative signal with a dissymmetry factor (g_{lum}) of −0.34, representing a clear inversion of handedness compared to the undoped **Br10Ch** (g_{lum} = +0.30; Fig. 4b).

The observed inversion in CPL handedness (from g_{lum} = +0.30 in undoped **Br10Ch** to g_{lum} = −0.34 in the doped system) arises from the selective reflection mechanism of the left-handed N* LC phase.[51–54] In the undoped system, the CPL handedness is primarily governed by optical rotation, where

emitted light follows the helical twist of the N* axis, resulting in left-handed polarization. Upon doping with 8CNS, guest-induced swelling increases the helical pitch of the N* phase, shifting the selective reflection band to 450–500 nm (Fig. 5d). This band now closely overlaps with the 8CNS emission maximum at 502 nm. As a result, left-handed CPL from the fluorophore is selectively reflected by the cholesteric matrix, while right-handed CPL is transmitted (Fig. 5f). The reflectance spectrum (Fig. S11) confirms this effect, showing a reflection band centered at 508 nm—nearly matching the emission wavelength. This spectral overlap between emission and reflection bands leads to the inversion of observed CPL handedness and demonstrates a unique mechanism of handedness switching through selective reflection and helical amplification, offering a versatile strategy for dynamically tunable CP-emissive systems.

Conclusion

In summary, we have demonstrated a high-performance, purely organic CPP system based on brominated cholesteric liquid crystals (Br(*n*)Ch), capable of self-assembling into left-handed N* phases. Among them, **Br10Ch** showed exceptional blue CPP performance with a high phosphorescent quantum yield (36%) and dissymmetry factor (g_{lum} = +0.30). This behavior results from the synergistic effects of enhanced spin–orbit coupling and supramolecular helical order that suppress non-radiative decay. Importantly, doping **Br10Ch** with an achiral fluorophore (8CNS) enabled green CPF *via* triplet-to-singlet FRET, accompanied by inversion of CPL handedness (g_{lum} = −0.34) due to selective reflection within the N* matrix. These findings establish a modular and tunable strategy for achieving efficient CP-RTP emission in organic systems, offering new design avenues for advanced chiral photonic devices. The use of cholesteric LCs as supramolecular scaffolds highlights the potential of liquid crystalline order in directing optical anisotropy and improving triplet-state harvesting. Furthermore, our demonstration of CPL handedness inversion *via* structural modulation provides a foundation for dynamic optical control. This study contributes a significant advancement in the rational design of purely organic chiroptical phosphors and opens possibilities for future applications in displays, data encryption, sensing, and other optoelectronic technologies.

Author contributions

J.-M. H. and J. K. conceived and supervised the project. J.-M. H. and J. P. synthesized and characterized the investigated compounds. The (TD-)DFT calculations were conducted and analysed by J.-M. H. J.-M. H. wrote and J. K. edited this manuscript.

Conflicts of interest

The authors declare no competing financial interests.

Data availability

Supplementary information (SI): the experimental details, including synthesis procedures, characterization methods, and supporting data, are provided. See DOI: **https://doi.org/10.1039/d5qm00520e**.

Acknowledgements

We acknowledge the financial support from the START grant provided by the College of Engineering at the University of Michigan.

References

1 J. Han, S. Guo, H. Lu, S. Liu, Q. Zhao and W. Huang, Recent Progress on Circularly Polarized Luminescent Materials for Organic Optoelectronic Devices, *Adv. Opt. Mater.*, 2018, **6**, 1800538.
2 G. Long, R. Sabatini, M. I. Saidaminov, G. Lakhwani, A. Rasmita, X. Liu, E. H. Sargent and W. Gao, Chiral-perovskite optoelectronics, *Nat. Rev. Mater.*, 2020, **5**, 423–439.
3 Q. Song, J. Yang, K. Zheng, T. Zhang, C. Yuan, L. M. Yuan and X. Hou, Chiral Memory in Dynamic Transformation from Porous Organic Cages to Covalent Organic Frameworks for Enantiorecognition Analysis, *J. Am. Chem. Soc.*, 2024, **146**, 7594–7604.
4 Y. Wang, J. Xu, Y. Wang and H. Chen, Emerging chirality in nanoscience, *Chem. Soc. Rev.*, 2013, **42**, 2930–2962.
5 X. Zhan, F. F. Xu, Z. Zhou, Y. Yan, J. Yao and Y. S. Zhao, 3D Laser Displays Based on Circularly Polarized Lasing from Cholesteric Liquid Crystal Arrays, *Adv. Mater.*, 2021, **33**, 2104418.
6 M. Zhang, Q. Guo, Z. Li, Y. Zhou, S. Zhao, Z. Tong, Y. Wang, G. Li, S. Jin, M. Zhu, T. Zhuang and S.-H. Yu, Processable circularly polarized luminescence material enables flexible stereoscopic 3D imaging, *Sci. Adv.*, 2023, **9**, eadi9944.
7 M. Silvi and P. Melchiorre, Enhancing the potential of enantioselective organocatalysis with light, *Nature*, 2018, **554**, 41–49.
8 S. Jiang and N. A. Kotov, Circular Polarized Light Emission in Chiral Inorganic Nanomaterials, *Adv. Mater.*, 2023, **35**, e2108431.
9 Y. Nagata and T. Mori, Irreverent Nature of Dissymmetry Factor and Quantum Yield in Circularly Polarized Luminescence of Small Organic Molecules, *Front. Chem.*, 2020, **8**, 448.
10 X. Zou, N. Gan, Y. Gao, L. Gu and W. Huang, Organic Circularly Polarized Room-Temperature Phosphorescence: Strategies, Applications and Challenges, *Angew. Chem., Int. Ed.*, 2025, **64**, e202417906.
11 G. Baryshnikov, B. Minaev and H. Agren, Theory and Calculation of the Phosphorescence Phenomenon, *Chem. Rev.*, 2017, **117**, 6500–6537.

12 O. Bolton, K. Lee, H. J. Kim, K. Y. Lin and J. Kim, Activating efficient phosphorescence from purely organic materials by crystal design, *Nat. Chem.*, 2011, **3**, 205–210.
13 J. Choi, H. Im, J.-M. Heo, D. W. Kim, H. Jiang, A. Stark, W. Shao, P. M. Zimmerman, G. W. Jeon, J. W. Jang, E. H. Hwang, S. Kim, D. H. Park and J. Kim, Microsecond triplet emission from organic chromophore-transition metal dichalcogenide hybrids *via* through-space spin orbit proximity effect, *Nat. Commun.*, 2024, **15**, 10282.
14 M. S. Kwon, D. Lee, S. Seo, J. Jung and J. Kim, Tailoring intermolecular interactions for efficient room-temperature phosphorescence from purely organic materials in amorphous polymer matrices, *Angew. Chem., Int. Ed.*, 2014, **53**, 11177–11181.
15 J.-M. Heo, J. Kim, M. I. Hasan, H. Woo, J. Lahann and J. Kim, Directed Chiral Self-Assembly of Purely Organic Phosphors for Room-Temperature Circularly Polarized Phosphorescence, *Adv. Opt. Mater.*, 2024, **12**, 2400572.
16 J.-M. Heo, V. P. Nguyen, M. Zheng, J. Park, Y. M. Paulus and J. Kim, Noninvasive Detection of Chorioretinal Hypoxia *via* Poly(lactic-*co*-glycolic acid) Nanoparticles Embedded with Purely Organic Phosphors, *Adv. NanoBiomed. Res.*, 2025, **5**, 2400153.
17 Y. Yu, M. S. Kwon, J. Jung, Y. Zeng, M. Kim, K. Chung, J. Gierschner, J. H. Youk, S. M. Borisov and J. Kim, Room-Temperature-Phosphorescence-Based Dissolved Oxygen Detection by Core-Shell Polymer Nanoparticles Containing Metal-Free Organic Phosphors, *Angew. Chem., Int. Ed.*, 2017, **56**, 16207–16211.
18 Y. Zeng, V. P. Nguyen, Y. Li, D. H. Kang, Y. M. Paulus and J. Kim, Chorioretinal Hypoxia Detection Using Lipid-Polymer Hybrid Organic Room-Temperature Phosphorescent Nanoparticles, *ACS Appl. Mater. Interfaces*, 2022, **14**, 18182–18193.
19 W. Ye, Z. Meng, G. Zhan, A. Lv, Y. Gao, K. Shen, H. Ma, H. Shi, W. Yao, L. Wang, W. Huang and Z. An, High-Performance Circularly Polarized Phosphorescence by Confining Isolated Chromophores with Chiral Counterions, *Adv. Mater.*, 2024, **36**, e2410073.
20 W. Chen, Z. Tian, Y. Li, Y. Jiang, M. Liu and P. Duan, Long-Persistent Circularly Polarized Phosphorescence from Chiral Organic Ionic Crystals, *Chem. – Eur. J.*, 2018, **24**, 17444–17448.
21 X. Liang, T. T. Liu, Z. P. Yan, Y. Zhou, J. Su, X. F. Luo, Z. G. Wu, Y. Wang, Y. X. Zheng and J. L. Zuo, Organic Room-Temperature Phosphorescence with Strong Circularly Polarized Luminescence Based on Paracyclophanes, *Angew. Chem., Int. Ed.*, 2019, **58**, 17220–17225.
22 H. R. Fu, N. Wang, X. X. Wu, F. F. Li, Y. Zhao, L. F. Ma and M. Du, Circularly Polarized Room-Temperature Phosphorescence and Encapsulation Engineering for MOF-Based Fluorescent/Phosphorescent White Light-Emitting Devices, *Adv. Opt. Mater.*, 2020, **8**, 2000330.
23 W. Huang, C. Fu, Z. Liang, K. Zhou and Z. He, Strong Circularly-Polarized Room-Temperature Phosphorescence from a Feasibly Separable Scaffold of Bidibenzo[b,d]furan with Locked Axial Chirality, *Angew. Chem., Int. Ed.*, 2022, **61**, e202202977.
24 L. Gu, W. Ye, X. Liang, A. Lv, H. Ma, M. Singh, W. Jia, Z. Shen, Y. Guo, Y. Gao, H. Chen, D. Wang, Y. Wu, J. Liu, H. Wang, Y. X. Zheng, Z. An, W. Huang and Y. Zhao, Circularly Polarized Organic Room Temperature Phosphorescence from Amorphous Copolymers, *J. Am. Chem. Soc.*, 2021, **143**, 18527–18535.
25 R. Liu, B. Ding, D. Liu and X. Ma, Switchable circularly polarized Room-Temperature phosphorescence based on pure organic amorphous binaphthyl polymer, *J. Chem. Eng.*, 2021, **421**, 129732.
26 S. Fu, Y. Chen, Y. Xie and Z. Li, Photoactivated Circularly Polarized Room-Temperature Phosphorescence from Phenoselenazine Derivative and Its Application in Information Security, *Chin. J. Chem.*, 2024, **42**, 2499–2506.
27 F. Nie and D. Yan, Macroscopic Assembly of Chiral Hydrogen-bonded Metal-free Supramolecular Glasses for Enhanced Color-tunable Ultralong Room Temperature Phosphorescence, *Angew. Chem., Int. Ed.*, 2023, **62**, e202302751.
28 C. Xu, C. Yin, W. Wu and X. Ma, Tunable room-temperature phosphorescence and circularly polarized luminescence encoding helical supramolecular polymer, *Sci. China: Chem.*, 2021, **65**, 75–81.
29 L. Guang, Y. Lu, Y. Zhang, R. Liao and F. Wang, Circularly Polarized Phosphorescence of Benzils Achieved by Chiral Supramolecular Polymerization, *Angew. Chem., Int. Ed.*, 2024, **63**, e202315362.
30 S. An, L. Gao, A. Hao and P. Xing, Ultraviolet Light Detectable Circularly Polarized Room Temperature Phosphorescence in Chiral Naphthalimide Self-Assemblies, *ACS Nano*, 2021, **15**, 20192–20202.
31 L. Wang, A. Hao and P. Xing, Steroid-Aromatics Clathrates as Chiroptical Materials with Circularly Polarized Luminescence and Phosphorescence, *ACS Appl. Mater. Interfaces*, 2022, **14**, 44902–44908.
32 B. Chen, W. Huang and G. Zhang, Observation of Chiral-selective room-temperature phosphorescence enhancement *via* chirality-dependent energy transfer, *Nat. Commun.*, 2023, **14**, 1514.
33 J. H. Jiang, S. Zhao, Y. Sun and X. D. Wang, From Binary to Higher-Order Organic Cocrystals: Design Principles and Performance Optimization, *Angew. Chem., Int. Ed.*, 2025, **64**, e202507102.
34 M. Zeng, W. Wang, S. Zhang, Z. Gao, Y. Yan, Y. Liu, Y. Qi, X. Yan, W. Zhao, X. Zhang, N. Guo, H. Li, H. Li, G. Xie, Y. Tao, R. Chen and W. Huang, Enabling robust blue circularly polarized organic afterglow through self-confining isolated chiral chromophore, *Nat. Commun.*, 2024, **15**, 3053.
35 Y. Wu, M. Li, Z. G. Zheng, Z. Q. Yu and W. H. Zhu, Liquid Crystal Assembly for Ultra-dissymmetric Circularly Polarized Luminescence and Beyond, *J. Am. Chem. Soc.*, 2023, **145**, 12951–12966.
36 X. Wang, K. Yang, B. Zhao and J. Deng, Polymeric Cholesteric Superhelix Induced by Chiral Helical Polymer for

Achieving Full-Color Circularly Polarized Room-Temperature Phosphorescence with Ultra-High Dissymmetry Factor, *Small*, 2024, **20**, e2404576.

37 C. Yin, S. Sun, Z. A. Yan, H. Hu, P. Jiang, Z. Xu, H. Tian and X. Ma, A universal strategy for multicolor organic circularly polarized afterglow materials with high dissymmetry factors, *Proc. Natl. Acad. Sci. U. S. A.*, 2025, **122**, e2419481122.

38 S. Ma, H. Ma, K. Yang, Z. Tan, B. Zhao and J. Deng, Intense Circularly Polarized Fluorescence and Room-Temperature Phosphorescence in Carbon Dots/Chiral Helical Polymer Composite Films, *ACS Nano*, 2023, **17**, 6912–6921.

39 H. K. Bisoyi and Q. Li, Liquid Crystals: Versatile Self-Organized Smart Soft Materials, *Chem. Rev.*, 2022, **122**, 4887–4926.

40 Q. Fan, Z. Li, K. Jiang, J. Gao, S. Lin and J. Guo, Tunable circular polarization room temperature phosphorescence with ultrahigh dissymmetric factor by cholesteric liquid crystal elastomers, *Cell Rep. Phys. Sci.*, 2023, **4**, 101583.

41 W. Gong, G. Huang, Y. Yuan and H. Zhang, Strong and Multicolor-Tunable Pure Organic Circularly Polarized Room-Temperature Phosphorescence from Cholesteric Liquid Crystal, *Adv. Opt. Mater.*, 2023, **11**, 2300745.

42 W. Gong, M. Zhou, L. Xiao, C. Fan, Y. Yuan, Y. Gong and H. Zhang, Multicolor-Tunable and Time-Dependent Circularly Polarized Room-Temperature Phosphorescence from Liquid Crystal Copolymers, *Adv. Opt. Mater.*, 2023, **12**, 2301922.

43 Z. Huang, Z. He, B. Ding, H. Tian and X. Ma, Photoprogrammable circularly polarized phosphorescence switching of chiral helical polyacetylene thin films, *Nat. Commun.*, 2022, **13**, 7841.

44 X. Wang, B. Zhao and J. Deng, Liquid Crystals Doped with Chiral Fluorescent Polymer: Multi-Color Circularly Polarized Fluorescence and Room-Temperature Phosphorescence with High Dissymmetry Factor and Anti-Counterfeiting Application, *Adv. Mater.*, 2023, **35**, e2304405.

45 K. Wu, D. Liu, L. Zhu, T. Wu, Y. Xu, C. He, Y. Xiong, Z. Zhao and B. Z. Tang, Recent progress in triplet energy transfer systems toward organic afterglow materials, *Commun. Chem.*, 2025, **8**, 85.

46 A. Taugerbeck and C. Booth, Design and Synthesis of Chiral Nematic Liquid *Crystals, Handbook of Liquid Crystals*, Wiley, 2014.

47 J.-M. Heo, J. Park, M. F. Flórez-Angarita, L. Wang, C. Yu, J. Choi, H. Woo, B. Milián-Medina, A. J. Matzger, M. S. Kwon, J. Gierschner and J. Kim, Elucidating the molecular structural origin of efficient emission across solid and solution phases of single benzene fluorophores, *Nat. Commun.*, 2025, **16**, 5560.

48 L. Zang, W. Shao, O. Bolton, R. Ansari, S. J. Yoon, J.-M. Heo, J. Kieffer, A. J. Matzger and J. Kim, Polarity-induced dual room-temperature phosphorescence involving the T 2 states of pure organic phosphors, *J. Mater. Chem. C*, 2022, **10**(39), 14746–14753.

49 L. Wei, S. Guo, B. Zhang, B. Jiang, Y. Wang, Z. Liu, Y. Xu, Y. Gong, Y. Liu and W. Z. Yuan, Tuning Circularly Polarized Afterglow Color *via* Modulation of Energy and Chirality Transfer in Co-Doped Films, *Adv. Funct. Mater.*, 2024, **34**, 2409681.

50 S. Kuila and S. J. George, Phosphorescence Energy Transfer: Ambient Afterglow Fluorescence from Water-Processable and Purely Organic Dyes *via* Delayed Sensitization, *Angew. Chem., Int. Ed.*, 2020, **59**, 9393–9397.

51 X. Yang, X. Jin, T. Zhao and P. Duan, Circularly polarized luminescence in chiral nematic liquid crystals: generation and amplification, *Mater. Chem. Front.*, 2021, **5**, 4821–4832.

52 J. Yan, F. Ota, B. A. San Jose and K. Akagi, Chiroptical Resolution and Thermal Switching of Chirality in Conjugated Polymer Luminescence *via* Selective Reflection using a Double-Layered Cell of Chiral Nematic Liquid Crystal, *Adv. Funct. Mater.*, 2016, **27**, 1604529.

53 S. Lin, H. Sun, J. Qiao, X. Ding and J. Guo, Phototuning Energy Transfer in Self-Organized Luminescent Helical Superstructures for Photonic Applications, *Adv. Opt. Mater.*, 2020, **8**, 2000107.

54 B. A. San Jose, J. Yan and K. Akagi, Dynamic switching of the circularly polarized luminescence of disubstituted polyacetylene by selective transmission through a thermotropic chiral nematic liquid crystal, *Angew. Chem., Int. Ed.*, 2014, **53**, 10641–10644.